PSFC/JA-10-30

Development of a Synthetic Phase Contrast Imaging Diagnostic

J.C. Rost, L. Lin*, and M. Porkolab

August 2010

Plasma Science and Fusion Center
Massachusetts Institute of Technology
Cambridge, MA 02139 USA

*Present Address: University of California, Los Angeles, Los Angeles, CA 90095

This work was supported by the U.S. Department of Energy, Grant No. DE-FG02-94ER54235.

Submitted for publication to *Physics of Plasmas*

Development of a Synthetic Phase Contrast Imaging Diagnostic

J.C. Rost, L. Lin*, and M. Porkolab

Plasma Science and Fusion Center, Massachusetts Institute of Technology,
Cambridge MA 02139
*Present Address: University of California, Los Angeles, Los Angeles, CA 90095

Abstract

A "synthetic diagnostic" has been developed to calculate the expected experimental response of phase contrast imaging (PCI), a scattering diagnostic used to measure density fluctuations in laboratory plasmas, to a tokamak discharge modeled with the GYRO nonlinear gyrokinetic code [J. Candy and R. E. Waltz, J. Comput. Phys. **186**, 545 (2003)]. The synthetic PCI includes the spatial response of the experimental diagnostic, primarily implemented as a line integral of plasma density along the beam path, and the minimum and maximum wavenumber response resulting from the detection scheme. The synthetic PCI can be used for comparisons between GYRO and experiment as well as studies of the PCI response.

1 Introduction

An ever more important role in plasma research is being played by computer models of plasma turbulence which calculate the fluctuating plasma densities and potentials in tokamaks in the wavenumber and frequency range believed to cause particle and energy transport, $k\rho_e < 1$ and $\omega < \omega_{ci}$.[1] The models can help illuminate the underlying physics of transport, for example the correlation between the level of transport and the fluctuation amplitude[2] and the relative phase[3] or the contribution to transport by instabilities at different spatial scales.[4] A computer model has two advantages over an experiment. First, the models are easier to diagnose than the experimental plasmas, both because some fields, such as the potential, are difficult to measure experimentally and because the model permits an arbitrary number of samples at any spatial scale. Second, bulk plasma parameters such as the density and temperature can be varied individually and precisely in a simulation but can only be controlled indirectly in an experiment. Another role of models in plasma research lies in prediction. It is critical that design of large scale, high performance experiments such as ITER be based on accurate predictions of plasma performance.[5]

For reliable predictive capability, appropriate validation of the model is required;[6] that is to say a model must be shown to be consistent with physical experiments in the parameter range in which it is applied. The comparison of model results to experiment is not as simple as it would seem due to the limitations of experimental diagnostics. All plasma measurements have limits in wavenumber, frequency, and spatial response, and the instrumental response must be incorporated in any valid comparison between modeling and experiment. A "synthetic diagnostic"[7,8] applies the known instrumental response to the output of the computer model to calculate the signals that would be generated by the experimental diagnostic. The synthetic diagnostic data can then be analyzed as if it were experimental data

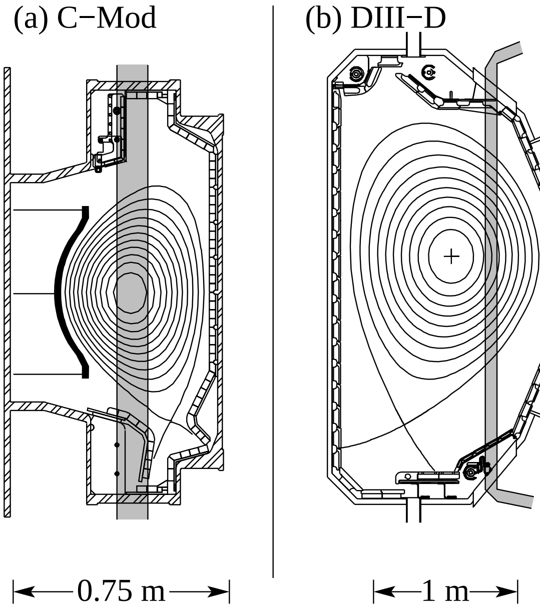

Figure 1: PCI beam paths on (a) Alcator C-Mod and (b) DIII–D are shown shaded on the machine cross section.

to find frequency spectra, correlation lengths, or other parameters as appropriate for the diagnostic, the result of which can be used for direct, quantitative comparisons between the model and experiment.

Interpretation of the results of phase contrast imaging (PCI) benefits significantly from the synthetic diagnostic approach. As described below, PCI effectively integrates the path of a laser beam through the plasma[9] (shown in Fig. 1). While several assumptions are required to estimate parameters such as total fluctuation amplitude $\tilde{n}$ or correlation length from PCI measurements,[10] a comparison of PCI results with modeling results can be made using a synthetic diagnostic without making these questionable assumptions.

Not every model provides output suitable for a synthetic PCI (SPCI). The model must cover the large radial and poloidal extent of the plasma traversed by the PCI beam path. The range of the model must extend beyond the wavenumber range expected for ion thermal gradient (ITG) and trapped-electron mode (TEM) instabilities into the range of electron thermal gradient (ETG) instabilities to match the wavenumber range of the PCI diagnostics on DIII–D[11] and Alcator C-Mod.[12] The model determined to best fit these requirements is the nonlinear gyrokinetic code GYRO.[13–15] It includes the full gyrokinetic response of both electrons and ions, electromagnetic effects, plasma shaping, and can use experimental profiles for plasma parameters.

Synthetic diagnostics are best implemented as post processors. That allows for separate development of the model and synthetic diagnostic and permits many synthetic diagnostics to be applied to the output of each relatively costly model run. Several synthetic diagnostics exist for use with GYRO.[7,8]

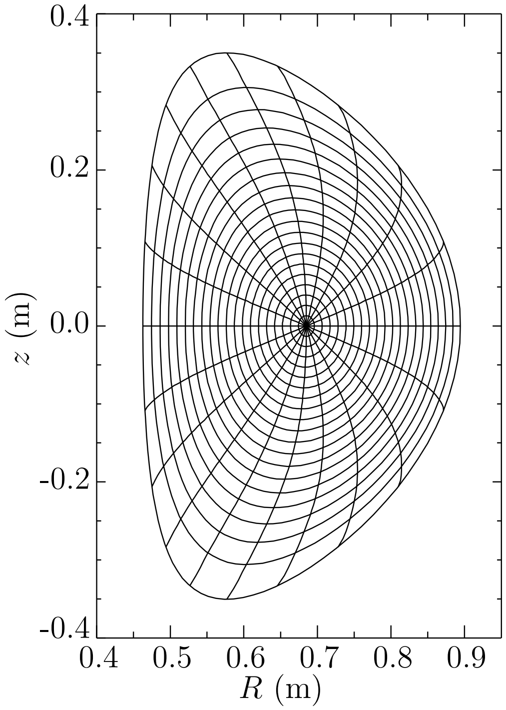

Figure 2: Miller coordinate system for a GYRO simulation of a C-Mod discharge. Flux surfaces are spaced by 0.05 in r/a. Spacing of θ coordinates is $2\pi/20$.

Section 2 of this paper describes the calculations that constitute the synthetic PCI diagnostic. Section 3 provides an example of the SPCI applied to a simulation of a plasma typical of Alcator C-Mod.

2 Components of the SPCI Calculation

2.1 Plasma Geometry

GYRO does not allow a completely free representation of the flux surfaces. Instead, the Miller Geometry[16] is assumed, which ensures that the plasma is in MHD equilibrium. An approximate Miller Geometry representation must be determined for the plasma to be simulated. This is provided by codes such as TRANSP[17] and ONETWO.[18] The Miller flux surfaces for a simulation of C-Mod are shown in Fig. 2. In the Miller representation, each flux surface is parametrized as

$$R = R_0 + r\cos(\theta + \sin^{-1}\delta\sin\theta), \tag{1}$$

$$z = \kappa r \sin\theta. \tag{2}$$

The terms R_0, δ, κ, and r vary across the plasma profile. For simplicity, each flux surface can be labeled with its value of r, and R_0, δ, and κ then become functions of r. A term δ_1 describing up-down asymmetry in triangularity is also included in GYRO, but as it has minimal effect on the part of the plasma concerning the SPCI it is not considered here. The parameters $R_0(r)$, $\delta(r)$, and $\kappa(r)$ are provided as values at a discrete set of points. In practice, the set of points is dense enough (*e.g.* 50 points across the plasma column) that a piece-wise linear interpolation is adequate for the SPCI. Note that θ is a dummy parameter and not a physical angle, *i.e.* $\theta \neq \tan^{-1}(z/(R - R_0))$ except for plasmas with circular cross-section.

The position of the PCI beam path is fixed in lab space but not in Miller coordinates, because the geometry of each plasma varies. It is necessary therefore to invert the relations in Eqs. 1 and 2 to determine the values of r and θ that correspond to a point (R,z) in lab space. This calculation is trivial to describe but not to implement. The set of equations cannot be inverted directly both because the θ dependence is complex and because the interpolated functions $R_0(r)$, $\delta(r)$, and $\kappa(r)$ are not analytic. In restricted portions of the plasma, for example near the midplane (*i.e.* $\theta = 0$), approximations may be used to simplify the calculation, but the SPCI must be accurate for all values of θ. The values of R and z must be determined to an accuracy much better than 1 mm to allow the SPCI to accurately represent wavenumbers as high as 40 cm^{-1} as appropriate for the experimental diagnostics.

The inversion is accomplished by first defining a distance function

$$D(r,\theta) = \left[(R_1 - R(r,\theta))^2 + (z_1 - z(r,\theta))^2\right]^{1/2}, \tag{3}$$

where $R(r,\theta)$ and $z(r,\theta)$ are defined in Eq. 1 and Eq. 2. Then a minimization procedure is applied to the square of D, thereby finding the values of r and θ that correspond to the lab coordinates (R_1, z_1). Minimization is applied to the square of D because that quantity is roughly quadratic near the minimum.

It is important to note the manner in which the parameter δ can introduce errors into the calculation. Miller approximations of experimental plasma geometries may show a large amount of “noise,” or spurious oscillations, in the fit to $\delta(r)$ because the flux surface shape is insensitive to small changes in δ. This is equivalent to extremely large short-scale variations in plasma current, which has little effect on the shape of the flux surfaces or the GYRO simulation, but distorts the geometry mapping described here and hence the reconstruction of the fluctuating density. The parameter $\delta(r)$ resulting from the fits must be monitored and adjusted if necessary.

2.2 Density Reconstruction

The PCI measurement is sensitive to electron density, so the SPCI requires a calculation of the fluctuating density $\tilde{n}_e$ at arbitrary (r,θ) in the plasma. GYRO calculates the fluctuating density as a series of toroidal modes with explicit spatial dependence. For each mode ℓ, a complex envelope function $\delta n_\ell(r,\theta,t)$ is evolved nonlinearly. The outputs of GYRO include a file storing the geometrical phase $\nu(r,\theta)$ and a file with the density moments $\delta n_\ell(r,\theta,t)$ for all ℓ, r, θ, and t for each plasma species. The fluctuating density is calculated as[8,13]

$$\tilde{n}(r,\theta,\phi,t) = \bar{n}_e \sum_{\ell=-(N-1)}^{N-1} \delta n_\ell(r,\theta,t) e^{-i\ell(\phi+\nu(r,\theta)+\omega_0 t)}, \tag{4}$$

where $\bar{n}_e$ is a constant scale factor, N is the number of modes simulated, ω_0 is a rotation frequency, and the reality condition defines δn_ℓ for $\ell < 0$. The short-scale poloidal variation of the fluctuations comes from the phase of the exponential term. The rotation frequency produces the Doppler shift arising from plasma motion perpendicular to the magnetic field.

The plasma density must be determined at arbitrary (r, θ) while δn_ℓ and ν are known only on a grid. Because both the envelope functions δn_ℓ and the geometry function ν vary slowly with θ, a simple weighted average of the four nearest grid points is used to interpolate δn_ℓ and ν in r and θ,

$$\begin{aligned} H(r,\theta) = {} & w_r w_\theta H(r_i,\theta_j) + (1-w_r) w_\theta H(r_{i+1},\theta_j) \\ & + w_r(1-w_\theta) H(r_i,\theta_{j+1}) + (1-w_r)(1-w_\theta) H(r_{i+1},\theta_{j+1}), \end{aligned} \quad (5)$$

where $r_i < r < r_{i+1}$, $\theta_j < \theta < \theta_{j+1}$, $w_r = (r_{i+1} - r)/(r_{i+1} - r_i)$, $w_\theta = (\theta_{i+1} - \theta)/(\theta_{i+1} - \theta_i)$, and H is either ν or δn_ℓ. The density is constructed according to Eq. 4 using the interpolated values of ν and δn_ℓ. The given interpolation scheme has been found to produce a density $\tilde{n}$ which is smooth and undistorted, while interpolating the calculated values of $\tilde{n}$ leads to significant errors.

Performing the interpolated density reconstruction around the midplane on the high-field side of the plasma requires the proper symmetry and continuity relations. The geometric phase ν is antisymmetric in θ for up-down symmetric plasmas, and hence is discontinuous at $\theta = \pi$. The electron density $\tilde{n}_e$ is continuous at $\theta = \pi$ for all values of ϕ, so each term in the sum in Eq. 4 is continuous at $\theta = \pi$. These two relations permit the calculation of $\delta n_\ell(r, \theta = \pi, t)$ from $\delta n_\ell(r, \theta = -\pi, t)$.

2.3 Response of Phase Contrast Imaging

Phase contrast imaging (PCI) is an internal reference beam interferometry technique. Invented by Frits Zernike for microscopy, the application to tokamak plasmas was developed by H. Weisen.[9] The PCI method operates by turning the variation in the index of refraction in a probed medium into amplitude variation at an observation point. It is a small-angle scattering technique with the detector at an image plane. The experimental setup on DIII–D[19] is typical of installations on tokamak devices. A 5 cm diameter CO_2 laser beam at $\lambda_0 = 10.6\ \mu$m is used to probe the plasma.[11] The laser passes through the plasma nearly vertically. The laser is imaged onto a 16 channel HgMnTe detector with circular elements. The detector bandwidth is roughly 10 MHz, higher than the typical signals of interest (< 1 MHz). The Alcator C-Mod[20] PCI system[21] is similar.

In the plasma, the wave fronts of the electric field of the probe beam are distorted by density fluctuations,[9]

$$E_{\mathrm{pl}} = E_0 e^{i\Delta(\bar{R},t)} \simeq E_0(1 + i\Delta(\bar{R},t)), \quad (6)$$

where $\bar{R}$ is a coordinate perpendicular to the beam. PCI can generate a 2d image, but electrostatic turbulence in tokamaks shows little variation along the field lines, hence PCI is often implemented as a 1d diagnostic. The coordinate $\bar{R}$ is identical to the radial coordinate R for a purely vertical probe beam. The term E_0 includes effects that can be neglected for the current calculation, including the intensity profile of the beam and the phase shift due to propagation. The wavelength of the probe beam is chosen so that $\Delta \ll 1$.

In the detection system, an optical element called a phase plate is used to shift the phase of the unscattered radiation by $\pi/4$. The phase plate used on DIII–D is a 5 cm diameter ZnSe disk. The disk has a reflective coating with a thickness $\lambda_0/8$ except over an uncoated central region. The most weakly scattered radiation cannot be separated from the unscattered beam, leading to a loss of response at small wavenumbers. The nature of this cutoff has been calculated and the behavior verified in the laboratory.[22] The response has the functional form

$$T(k) = 1 - e^{-(k/k_{\min})^2}, \tag{7}$$

where $k_{\min}$ depends on physical parameters of the optical system. The discussion below assumes that this cutoff is applied.

The radiation with the unscattered component phase shifted by the phase plate is then imaged on the detector with magnification M creating an electric field

$$E_{\mathrm{det}}(M\bar{R}, t) = E_0(i + i\Delta(\bar{R}, t)). \tag{8}$$

The detector is sensitive to intensity,

$$I_{\mathrm{det}} = |E_{\mathrm{det}}|^2 = |E_0|^2|i + i\Delta|^2 \simeq |E_0|^2(1 + 2\Delta(\bar{R}, t)). \tag{9}$$

The detectors are a.c. coupled, so the detected intensity is proportional to the phase shift Δ. The beam size at the detector plane is larger than the detector, so variation in amplitude across the beam can be neglected or easily normalized out.

The phase shift Δ results from the index of refraction of the plasma, which is

$$N = (1 - \omega_{pe}^2/\omega^2)^{1/2} \simeq 1 - \omega_{pe}^2/2\omega^2 \tag{10}$$

for a CO_2 laser beam with frequency ω. The phase shift is thus related to the plasma frequency,

$$\Delta(\bar{R}) = k_0 \int (N - 1) d\bar{z} = -\int \omega_{pe}^2/(2c\omega) d\bar{z}, \tag{11}$$

where k_0 is the wavenumber of the laser beam and $\bar{z}$ describes length along the beam path. Using the definition of plasma frequency $\omega_{pe}^2 = n_e e^2/\epsilon_0 m_e$ and Eqs. 9 and 11, the time-dependent intensity at the detector is

$$\tilde{I}_{\mathrm{det}} \propto \int \tilde{n}_e(\bar{R}, \bar{z}) d\bar{z}. \tag{12}$$

2.4 Assembling the SPCI Signal

The equations presented in the previous sections are combined in a straightforward fashion to create the SPCI. The calculation simply integrates the intensity at the detector plane as described by Eq. 12 over each detector element. A set of chords parallel to the probe beam is chosen, spanning the width of the probe beam with a spacing of less than 1/4 of the detector element spacing. In the coordinate system used, each chord corresponds to a single value of $\bar{R}$. A set of points along each chord is chosen with a spacing $\Delta\bar{z}$ smaller than the shortest wavelength mode included in the simulated data.

For each point $(\bar{R}, \bar{z})$ in each chord, the corresponding (R, z) is used to calculate the Miller coordinate (r, θ) as described in Sec. 2.1. The fluctuating electron density is calculated at each (r, θ) in the PCI beam path as described in Sec. 2.2. The line integral along the beam path described by Eq. 12 is calculated as a sum over $\bar{z}$. The appropriate low k response is included by performing a Fourier Transform in $\bar{R}$ and multiplying by the response described by Eq. 7. The result is the intensity as a function of position across the detector.

The signal from each detector element is then calculated by performing an integral of the intensity over the area of the element. Detector elements on the DIII–D PCI are circular while the Alcator C-Mod PCI uses a detector with rectangular elements. The shape of the detector elements controls the system response above the highest resolvable wavenumber. Aliasing is not a problem in practice as the plasma turbulence spectrum falls off quickly with increasing k; optical antialiasing apertures can be added easily to the experimental PCI and incorporated into the SPCI as a high k cutoff to the transfer function in Eq. 7.

The resulting signals are stored in the format used for experimental PCI data so that the same routines are used for analysis of SPCI data as are used for experimental PCI data. The SPCI is implemented in the high-level computer language IDL,[23] commonly used in fusion research, as are most of the data analysis routines. The calculation can be speeded up when accurate response at the wavenumber limits is not needed by reducing the number of chords. The span of the chords can be limited to the portion of the beam imaged on the detector instead of the entire beam width at the loss of accurate low k response. The chord spacing can be increased to one chord per detector element when no high k modes are present in the simulation and correct modeling of the high k response is not needed. In practice, the speed difference is two orders of magnitude.

2.5 Verification of the SPCI

Verification of a model consists of establishing that a calculation accurately implements the underlying mathematical equations.[6] Each stage of the SPCI was analyzed separately to find any errors in the implementation. The inversion of the mapping described in Sec. 2.1 was tested to ensure that mapping $(R, z) \rightarrow (r, \theta) \rightarrow (R', z')$ reproduces the initial value. The inversion was also tested to verify that a continuous path in (R, z) space produces a continuous path in (r, θ) space. Calculation of the density reconstruction described in Sec. 2.2 was tested by implementing it twice in two independent pieces of code. First, the density was calculated for the entire simulated region on the given r grid and interpolated in θ. This is primarily for visualization. Second, the fluctuating density was calculated in a separately written piece of code on a rectangular grid in (R, z) to create a contour plot which was compared to the results from the visualization code. The calculation was also tested by checking that $\tilde{n}$ calculated along a continuous path in (R, z) is also continuous. The spectrum $S(k, f)$ resulting from the SPCI calculation was compared to the 2d spectra $S(k_r, k_\theta, f)$ calculated at several points along the beam path. Only the portions of the 2d spectra at $\mathbf{k} \perp \hat{z}$ (for a PCI beam in the $\hat{z}$ direction) contribute to the SPCI spectrum; a sum of these must have the same characteristics as the SPCI spectrum.

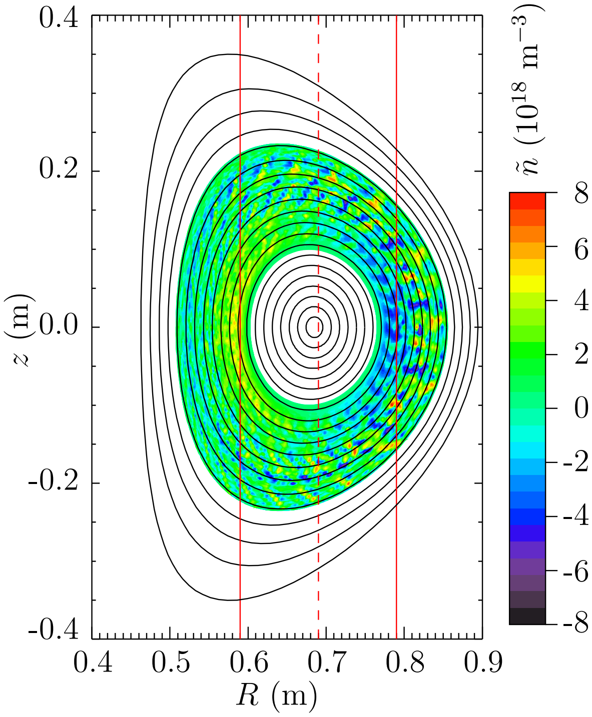

Figure 3: A reconstruction of fluctuating electron density $\tilde{n}_e$ for a typical GYRO run. This is performed on a simple grid for visualization purposes. The vertical red lines represent the PCI beam path.

3 Example of the SPCI Applied to a Simulation of Alcator C-Mod

The SPCI was written to apply equally well to the PCI diagnostics on Alcator C-Mod and DIII–D. Most of the required information is included in the GYRO output, but additional parameters of the PCI system are required; endpoints for the PCI laser path, the beam width, the number of detector channels, the channel spacing, the detector element shape, the optical magnification, and $k_{\min}$. The SPCI has been applied recently to model C-Mod plasmas during studies of transport in both L-mode plasmas[24] and H-mode plasmas.[25] The examples shown here are taken from the study of transport in H-mode plasmas. Complete details on the plasma parameters and the experimental PCI measurements are available in Ref. 25.

A reconstruction of the density fluctuations as predicted by GYRO for the C-Mod H-mode plasmas studied is shown in Fig. 3. The PCI beam path is shown at its maximum width. The simulation covers the region $0.38 < r/a < 0.80$ of a plasma with parameters $T_{e0} = T_{i0} = 1.4$ keV, $n_{e0} = 2.3 \times 10^{20}$ m^{-3}, $B_0 = 4.5$ T, $I_p = 0.8$ MA, with 2 MW of off-axis ICRF heating at 80 MHz. Two features indicate that the PCI signal above 200 kHz results from density fluctuations in the radial portion of the plasma included in the simulation. First, the phase velocity of the turbulence is close to the measured $E \times B$ velocity both

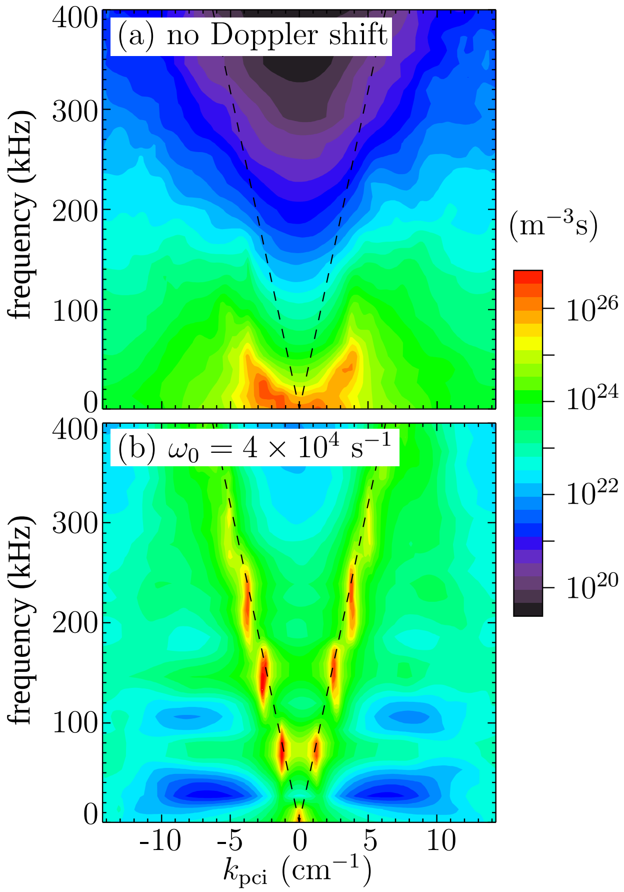

Figure 4: The spectrum $S(k_{\rm pci}, f)$ from a SPCI calculation applied to a GYRO simulation of a C-Mod discharge. (a) No Doppler shift added. (b) Rotation frequency $\omega_0 = 4 \times 10^4$ s^{-1} is applied, equivalent to a perpendicular plasma flow velocity of approximately $V_\perp = 3.2$ km/s at the measurement location. Dashed line represents a phase velocity of 4 km/s.

before and after the internal transport barrier forms. The Doppler shift of turbulence near the plasma edge is lower, hence it doesn't contribute significantly to the PCI signal at high frequency. Second, the spatial localization filter is able to localize the signal to the upper or lower plasma as shown below, and neither turbulence near the midplane nor turbulence near the last closed flux surface can be localized due to the magnetic geometry.

The SPCI spectrum $S(k_{\rm pci}, f)$ constructed from this GYRO simulation is shown in Fig. 4. Parameters of the Alcator C-Mod PCI are used: 32 channels, $k_{\rm min} = 0.5$ cm^{-1}, channel spacing in plasma 2.2 mm (for $k_{\rm max} = 14$ cm^{-1}), CO$_2$ beam diameter 0.11 m. The wavenumber $k_{\rm pci}$ refers to the direction perpendicular to the PCI beam; on C-Mod, this is $-\hat{R}$. No Doppler shift is applied in Fig. 4a, while a rotation frequency ω_0 as defined in Eq. 4 is added in Fig. 4b to match simulated and observed spectra. The Doppler shift is consistent with experimental observations of E_r.[25] Several features are seen that are typical of both the SPCI and experimental PCI data. The spectra show modes propagating with both posi-

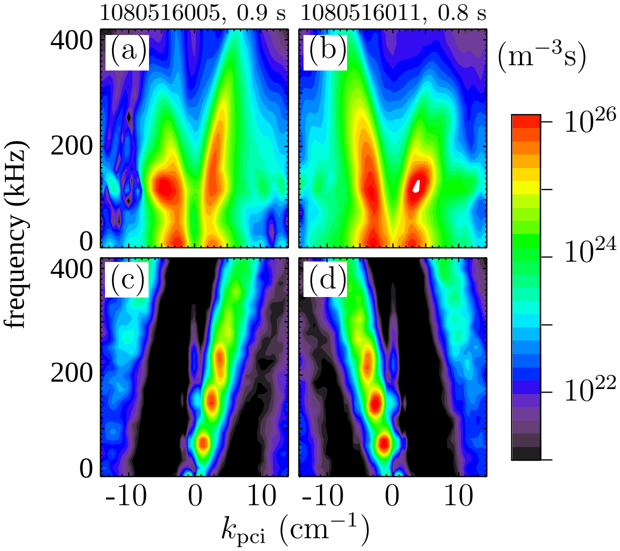

Figure 5: Experimental PCI spectra from two similar plasmas with either the responsivity localized in either the (a) lower or (b) upper portion of the tokamak. The SPCI spectra are shown limited to (c) $z < 0$ and (d) $z > 0$.

tive and negative k. At each frequency, the spectra peak at finite k, with the value of the wavenumber at the peak increasing with frequency. The turbulence has an intrinsic phase velocity of roughly 1 km/s so that the observed phase velocity in the lab frame of 4 km/s does not equal precisely the plasma $E \times B$ velocity.

The PCI was operated with a rotatable mask as an optical filter that allows a degree of spatial localization. The PCI response on two similar shots is shown in Fig. 5 with the filter set to select for the lower portion of the plasma in (a) and the upper in (b). The strong peak at 140 kHz is the quasicoherent (QC) mode.[26] The change in the broadband turbulence from $k < 0$ in the upper plasma to $k > 0$ in the lower indicates that the mode propagates in the ion diamagnetic drift direction. The SPCI signal can be artificially split at $z = 0$, separating the contribution from the lower plasma in (c) and from the upper in (d). The low-wavenumber spatial response of the localized PCI is similar to the size of the plasma minor radius, so a proper model of the observed signal includes a weighted integral over the whole plasma. The resulting SPCI spectrum and experimental spectrum are compared in Fig. 6. That wavenumber spectra of the model and experiment have been shown to match well in shape and absolute magnitude.[25] As is shown in Fig. 7. The frequency spectrum of the Doppler-shifted SPCI matches the experimental spectrum within a factor of two, except for irregularities at low f which could be remedied be rerunning the simulation with more modes at low n.

The data output by GYRO can be used to shed light on the physics underlying the PCI measurement through comparison of the SPCI results with a local parametrization of the turbulence. For example, the density reconstruction used for the SPCI can also be used to sample the simulated plasma on a 2d grid, allowing the calculation of the the local

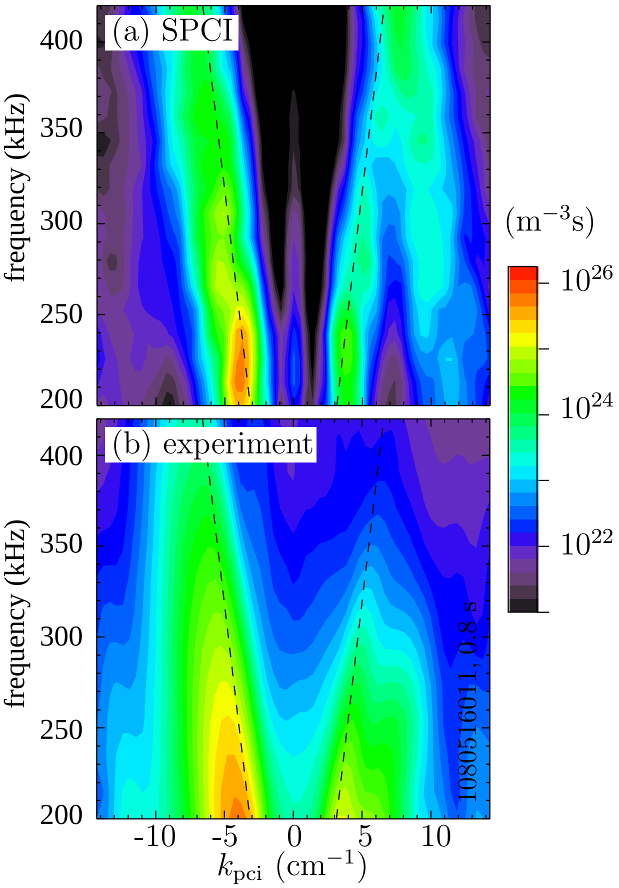

Figure 6: The broadband turbulence at high frequency of the (a) SPCI and (b) experimental PCI with the spatial localization filter selecting for the upper plasma. Dashed represents a phase velocity of 4 km/s. Note suppressed zero on frequency scale.

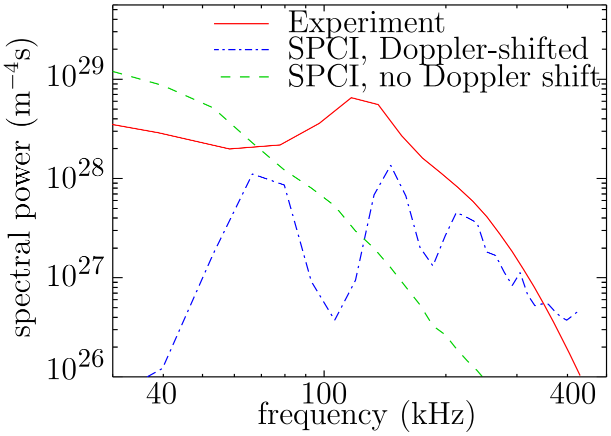

Figure 7: Frequency spectra of the experimental PCI (solid red line), SPCI including Doppler shift (dash-dot blue line), and SPCI with no Doppler shift (dashed green line). Peak in experimental spectrum at 140 kHz is due to the QC mode. Increasing the number of low-n modes in the GYRO simulation would smooth out the SPCI spectrum at low f but not change the overall power.[27]

2d spectrum $S(k_r, k_\theta)$ in the portion of the simulated region measured by the PCI beam ($R = 0.69$ m, $z = 0.15$ m), shown in Fig. 8 for a frequency of 200 kHz. As expected from the PCI signal, a peak is seen at $k_\theta = 4$ cm^{-1}. In the radial direction, the turbulence peaks at $k_r = 2$ cm^{-1} while the PCI responds only to turbulence with $k_r \simeq 0$ in this portion of the plasma, showing the difficulty in using the PCI to estimate total turbulence amplitude without aid of a model and SPCI. (The spectrum of turbulence is approximately symmetric in k_r near the midplane.) This data can be used to test methods for estimating turbulence amplitude from PCI signals. The standard estimation of PCI signal amplitude over a plasma column of length H measuring turbulence with correlation length L_c is $A = \tilde{n}_e\sqrt{HL_c}$.[10] The measured values used in the estimation are PCI signal amplitude $A = 2 \times 10^{16}$ m^{-2} between 300 and 500 kHz, path length of 0.23 m (half the machine size because the optical filter is in place), $L_c = 3$ mm at high frequency based on the observed spectrum, giving $\tilde{n}_e = A/\sqrt{HL_c} = 7 \times 10^{17}$ m^{-3}. The local turbulence amplitude from the GYRO reconstruction, filtered to include the appropriate frequency range, is 1×10^{18} m^{-3}, showing good agreement. This relation should be examined for a wider set of simulated plasmas. The probe beam of the C-Mod PCI is nearly perpendicular to the flux surfaces in the portion of the plasma simulated here, allowing the PCI wavenumber to be interpreted as k_θ. The DIII–D PCI beam, on the other hand, is at 45° to the outer flux surfaces; the SPCI is extremely valuable in interpreting the PCI signal in terms of k_r and k_θ for this machine.

4 Conclusions

A synthetic phase contrast imaging (SPCI) diagnostic has been implemented as a post processor for the GYRO gyrokinetic plasma fluctuation simulation. The SPCI includes the PCI spatial response by integration of the modeled fluctuating density, thereby including all ef-

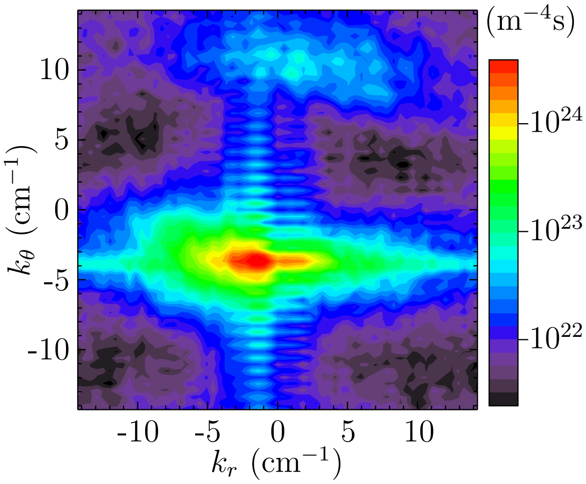

Figure 8: Two-dimensional power spectrum $S(k_r, k_\theta)$ at $f = 200$ kHz calculated from GYRO simulation data. Fluctuating density sampled at $R = 0.69$ m, $z = 0.15$ m on a 32×32 grid with a spacing of 2.2 mm.

fects of plasma geometry and turbulence characteristics. The wavenumber limits caused by the imaging and detection system are included with proper fall off. The SPCI is currently in use for comparing GYRO results with experiment on DIII–D and Alcator C-Mod.

The SPCI implementation has been written to be modular to maximize the adaptability of the code. The bulk of the code provides the fluctuating density $\tilde{n}_e$ at an arbitrary (R, z) anywhere in the plasma cross section. This portion of the SPCI code can be reused without modification in another synthetic diagnostic that can express its response as a function of $\tilde{n}_e(R, z)$.

The separation of the components of the SPCI can serve as a model for a general framework to be used in the development of synthetic diagnostics. One layer translates the output of the model to physical parameters in the lab frame, exposing this data through a standard interface. This code would be specific to the model. Synthetic diagnostics would be written to use the standard interface. Thus a synthetic diagnostic once written could be applied to the output of any model. This would maximize code reuse and increase the number of comparisons between model and experiment. It is an open question whether a standard interface as described could adequately support the full range of diagnostic needs. This issue will be explored as the SPCI is adapted to spatially localized PCI.[11]

Acknowledgments

This work is supported by the U.S. DOE under DE-FG02-94-ER54235. This research utilized parallel computational clusters at MIT Plasma Science and Fusion Center (Loki) and Princeton Plasma Physics Laboratory (Kestrel). The authors wish to thank Jeff Candy and Ron Waltz for creating GYRO and for advice and assistance in this work.

References

[1] ITER Physics Expert Group on Confinement and Transport, ITER Physics Expert Group on Confinement Modelling and Database, and ITER Physics Basis Editors, Nucl. Fusion **39**, 2175 (1999).

[2] R. E. Waltz, G. D. Kerbel, and J. Milovich, Phys. Plasmas **1**, 2229 (1994).

[3] C. F. Figarella, S. Benkadda, P. Beyer, X. Garbet, and I. Voitsekhovitch, Phys. Rev. Lett. **90**, 015002 (2003).

[4] J. Candy, R. E. Waltz, M. R. Fahey, and C. Holland, Journal of Physics: Conference Series **78**, 012008 (2007).

[5] M. Shimada, D. J. Campbell, V. Mukhovatov, M. Fujiwara, N. Kirneva, K. Lackner, M. Nagami, V. D. Pustovitov, N. Uckan, J. Wesley, N. Asakura, A. E. Costley, A. J. H. Donne, E. J. Doyle, A. Fasoli, C. Gormezano, Y. Gribov, O. Gruber, T. C. Hender, W. Houlberg, S. Ide, Y. Kamada, A. Leonard, B. Lipschultz, A. Loarte, K. Miyamoto, V. Mukhovatov, T. H. Osborne, A. Polevoi, and A. C. C. Sips, Nucl. Fusion **47**, S1 (2007).

[6] P. W. Terry, M. Greenwald, J.-N. Leboeuf, G. R. McKee, D. R. Mikkelsen, W. M. Nevins, D. E. Newman, D. P. Stotler, Task Group on Verification and Validation, U.S. Burning Plasma Organization, and U.S. Transport Task Force, Phys. Plasmas **15**, 062503 (2008).

[7] R. V. Bravenec and W. M. Nevins, Rev. Sci. Instrum. **77**, 015101 (2006).

[8] C. Holland, A. E. White, G. R. McKee, M. W. Shafer, J. Candy, R. E. Waltz, L. Schmitz, and G. R. Tynan, Phys. Plasmas **16**, 052301 (2009).

[9] H. Weisen, Plasma Phys. Control. Fusion **28**, 1147 (1986).

[10] S. C. Coda, M. Porkolab, and K. H. Burrell, Phys. Letters A **273**, 125 (2000).

[11] J. R. Dorris, J. C. Rost, and M. Porkolab, Rev. Sci. Instrum. **80**, 023503 (2009).

[12] L. Lin, E. M. Edlund, M. Porkolab, Y. Lin, and S. J. Wukitch, Rev. Sci. Instrum. **77**, 10E918 (2006).

[13] J. Candy and R. E. Waltz, J. Comput. Phys. **186**, 545 (2003).

[14] J. Candy and R. E. Waltz, Phys. Rev. Lett. **91**, 045001 (2003).

[15] R. E. Waltz, J. Candy, F. L. Hinton, C. Estrada-Mila, and J. E. Kinsey, Nuclear Fusion **45**, 741 (2005).

[16] R. L. Miller, M. S. Chu, J. M. Greene, Y. R. Lin-Liu, and R. E. Waltz, Phys. Plasmas **5**, 973 (1998).

[17] R. J. Goldston, D. C. McCune, H. H. Towner, S. L. Davis, R. J. Hawryluk, and G. L. Schmidt, J. Comput. Phys. **43**, 61 (1981).

[18] H. St. John, T. S. Taylor, Y. R. Lin-Liu, and A. D. Turbull, Proc. 15th Int. Conf. Plasma Phys. and Control. Nucl. Fusion Research, Seville, 1994 (IAEA, Vienna, 1995), Vol. 3, p. 603.

[19] J. L. Luxon, Nucl. Fusion **42**, 614 (2002).

[20] E. Marmar and the Alcator C-Mod Group, Fusion Sci. Tech. **51**, 261 (2007).

[21] M. Porkolab, J. C. Rost, N. Basse, J. Dorris, E. Edlund, L. Lin, Y. Lin, and S. Wukitch, IEEE Trans. Plasma Sci. **34**, 229 (2006).

[22] S. Coda, Ph.D. thesis, Massachusetts Institute of Technology, 1997.

[23] The Interactive Data Language, distributed by ITT Visual Informations Solutions, 4990 Boulder, CO (http://www.ittvis.com/idl/).

[24] L. Lin, M. Porkolab, E. M. Edlund, J. C. Rost, M. Greenwald, N. Tsujii, J. Candy, R. E. Waltz, and D. R. Mikkelsen, Plasma Phys. Control. Fusion **51**, 065006 (2009).

[25] L. Lin, M. Porkolab, E. M. Edlund, J. C. Rost, C. L. Fiore, M. Greenwald, Y. Lin, D. R. Mikkelsen, N. Tsujii, and S. J. Wukitch, Phys. Plasmas **16**, 012502 (2009).

[26] A. Mazurenko, M. Porkolab, D. Mossessian, J. A. Snipes, X. Q. Xu, and W. M. Nevins, Phys. Rev. Lett. **89**, 225004 (2002).

[27] C. Holland, J. Candy, R. E. Waltz, A. E. White, G. R. McKee, M. W. Shafer, L. Schmitz, and G. R. Tynan, Journal of Physics: Conference Series **125**, 012043 (2008).